Photocatalytic degradation of glyphosate using Ce/N co-doped TiO$_2$ with oyster shell powder as carrier under the simulated fluorescent lamp

Wei Zhang[1,2,3]*, Qizheng You[2], Jinkai Shu[1,3], Aihe Wang[1,3], Hai Lin[4] and Xuchao Yan[4]

[1]School of Municipal and Mapping Engineer, Hunan City University, Yiyang, Hunan, China, [2]School of Municipal and Environmental Engineering, Shenyang Jianzhu University, Shenyang, Liaoning, China, [3]Hunan Provincial Village Drinking Water Quality Safety Engineering Technology Research Center, Yiyang, Hunan, China, [4]Yiyang City Commodity Quality Supervision and Inspection Institute, Yiyang, Hunan, China

Glyphosate is currently one of the most used organophosphorus herbicides in the world and its accumulation and translocation in soil and wave causes environmental pollution and biological health problems. A new approach to the problem is provided by the preparation of cerium and nitrogen co-doped titanium dioxide composite nano-photocatalysts loaded on modified oyster shell powder (CeNT@Oys) by a simple hydrothermal synthesis. The physicochemical and optoelectronic properties are analyzed using SEM, BET, XRD, Raman, FTIR, UV-vis DRS, XPS characterization techniques and a range of photoelectrochemical techniques. The results show that the addition of modified oyster shell powder increases its specific surface area, while Ce-N-TiO$_2$ is an anatase crystal composed of Ce doped in the form of interstitial and surface, interstitial form of N, and the co-doping of Ce and N elements gives it the property of being excited by visible light. The photocatalytic activity of the different catalysts was evaluated by degrading 50 mg/L glyphosate solution under simulated sunlight. The catalyst was determined to be reusable by five repeated degradation experiments. Based on quenching experiments and the electron paramagnetic resonance tests, the effective active species of glyphosate degraded by the catalyst was determined and the mechanism of glyphosate degradation by photocatalyst was proposed. Finally, the degradation pathway for the photocatalytic degradation of PMG by CeNT@Oys was determined by HPLC-MS/MS determine of the intermediate products.

KEYWORDS

nitrogen and cerium, co-doped TiO$_2$, photocatalytic, glyphosate, oyster shell powder

1 Introduction

Glyphosate (N-phosphonomethylglycine, PMG), as the main active ingredient in many commercial herbicides (e.g., Roundup) (Annett et al., 2014; Gill et al., 2017), is a broad-spectrum inactivating, systemic conducting organophosphorus herbicide with the advantages of high efficiency, broad spectrum and low toxicity (Espinoza-Montero et al., 2020). The global studies have shown that glyphosate is widely contaminated in all types of aqueous environments including groundwater, surface water and seawater (Battgalin et al., 2005; Battaglin et al., 2014; Ruiz-Toledo et al., 2014).

Due to its high mobility and high water solubility (Bonansea et al., 2017), glyphosate enters the water cycle after application in the form of agricultural or urban runoff, rainwater washout (Villamar-Ayala et al., 2019), overspray (Hanke et al., 2010), and improper disposal of agricultural implements. In recent years, glyphosate has also been used in freshwater lakes to control malignant weeds such as hollow lily grass and water hyacinth, although glyphosate herbicides are not approved for use in the aquatic environments (Coupe et al., 2012; Villamar-Ayala et al., 2019), and has become one of the typical pesticide-based DOPs for phosphorus inputs to lakes, exacerbating the process of eutrophication in water bodies and damaging aquatic ecosystems.

According to medical studies (Samsel and Seneff 2013; Mesnage et al., 2015; Tarazona et al., 2017), glyphosate may be associated with a variety of human diseases, including cancer, psychiatric disorders and endocrine disorders, and has significant toxic effects on phytoplankton, fish and other aquatic organisms (Ma et al., 2019; Matozzo et al., 2019; Tresnakova et al., 2021). In 2015, PMG was reclassified as a class 2A carcinogen by the International Agency for Research on Cancer (IARC), a division of the World Health Organization (WHO) (Van Bruggen et al., 2018). Therefore, research into effective treatment methods to degrade DOP to DIP is necessary for PMG wastewater.

In recent years, nano-TiO_2-based non-homogeneous photocatalytic technology has been used to degrade PMG in water, and TiO_2 has attracted widespread attention due to its good properties such as high chemical stability, environmental friendliness and cheap accessibility. Unfortunately, the 3.20 eV forbidden band width of anatase TiO_2 limits its use to less than 5% of sunlight with wavelengths less than 375 nm in the ultraviolet (Ali et al., 2018), for another, the quantum yield of TiO_2 crystal is only about 4% and the photogenerated carriers have a high compounding rate. Therefore, how to modify TiO_2 nanoparticles to absorb visible light and reduce the photogenerated electron-hole pair complexation efficiency has been one of the top priorities of researchers studying photocatalysis in recent years.

It has been shown that co-doping of TiO_2 with metal and non-metal ions can not only inhibit the crystal transition of TiO_2 from rutile to anatase, reduce the size of nanoparticles, reduce electron-hole pair complexation, but achieve a response in the visible wavelength range (Khalid et al., 2017; Hu et al., 2019). Among them, cerium ions (Ce^{3+}/Ce^{4+}), one of the four most abundant rare Earth metals, are inexpensive and non-toxic, and are considered ideal dopants for modifying the TiO_2 crystal and electronic structure, changing optical properties and improving quantum yields (Makdee et al., 2018; Alipanahpour Dil et al., 2019; Maarisetty and Baral 2019). Similarly, doping the TiO_2 lattice with non-metallic elements such as C, N, S, F and Cl elements can successfully reduce the forbidden band width and red-shift the optical response range towards the visible region. Among them, N has high electronegativity and high ionisation energy, which can accelerate the rate of photocatalytic reactions (Sharotri et al., 2019; Sun et al., 2020).

Further, the stronger the photocatalyst's ability to adsorb pollutants, the easier it is for the active radicals to exert their degradation ability to attack organic molecules. Higher specific surface area or adjusted surface zero point energy can directly or indirectly increase the capacity of adsorption. Therefore, the combination of photocatalysts and highly efficient adsorbent materials to achieve adsorption-photocatalytic "cooperation" can also effectively increase photocatalytic efficiency. Currently, the use of waste materials to prepare new, inexpensive, "green" adsorbents is a hot topic of research (Abbas 2014; Jiang et al., 2018), such as quartz particles, fly ash, zeolite and other natural materials and waste slag-based adsorbent materials (Cao et al., 2018; Wang et al., 2018; Alvarez-García et al., 2019). The oyster is a highly productive and environmentally adaptable aquatic organism that absorbs elements from the surrounding environment and forms a shell with a carbonate composition through the secretion of its soft body, rich in $CaCO_3$ and a large number of micropores. It was found that the specific surface area of oyster shell powder was larger after modification and the pore size was mainly distributed in the range of 2 nm–10 nm, which could efficiently adsorb DOP from water bodies (Yu et al., 2010; Oladoja et al., 2015).

The double ion co-doped TiO_2 nanoparticles was loaded onto the modified oyster shell powder to optimize the photocatalytic material properties and thus improve the photocatalytic degradation efficiency, and was used for the adsorption-photodegradation of glyphosate. In our work, Modified oyster shell powder/Ce-N-TiO_2 (CeNT@Oys) composite nano-photocatalysts were prepared by hydrothermal synthesis and their physicochemical and optical properties were analysed. The photocatalytic degradation activity of CeNT@Oys photocatalysts for PMG was evaluated under simulated solar irradiation, and the effect on the degradation efficiency of glyphosate at different pH values were investigated, while its reusability was assessed by recycling samples for recycling study tests. In addition, the mechanism of photocatalytic degradation of glyphosate was proposed based on quenching experiments and EPR characterization, and the degradation pathway of glyphosate was estimated by analyzing the intermediate products.

2 Materials and methods

2.1 Materials and reagents

Discarded oyster shell, Glyphosate [N-(Phosphonomethyl) glycine, $C_3H_8NO_5P$, 95%] was from Shi-Feng Biotechnology Co., Ltd., Shanghai, PRC; Tetrabutyl orthotitanate (TBOT), Absolute ethanol (C_2H_5OH) as solvent, Cerium nitrate hexahydrate [$Ce(NO_3)_3 \bullet 6H_2O$] and urea (CH_4N_2O) were used as the precursor of cerium and nitrogen, respectively, hydrochloric acid (HCl). All chemicals were analytical grade purity and can be directly applied without any further treatment.

2.2 Preparation of modified oyster shell powder

The surface of the discarded oyster shells was removed with a steel wire ball, polished to a white colour with a cutting machine and cut into small pieces, dried in a blast oven at 65°C, crushed in a sealed sample miller for 3 min–5 min, sieved, soaked in 0.1% dilute hydrochloric acid, vacuum dried and calcined in a muffle furnace at 900°C to obtain modified oyster shell powder, which was sealed and stored.

2.3 Preparation of CeNT@Oys composite nano-photocatalyst

CeNT@Oys was prepared by a simple hydrothermal method in a typical procedure as follows: Solutions A was prepared by mixing

36 mL of anhydrous ethanol and a quantitative amount of modified oyster shell powder by ultrasonic shaking and then adding 10 mL of tetrabutyl titanate to it and stirring evenly. Solution B was then slowly added to Solution A at a rate of 1 drop/s and stirred for two hours at room temperature. To 120°C in a vacuum oven for 16 h and then removed and cooled, the resulting precipitate was filtered several times with deionised water and dried overnight at 60°C. To allow complete crystallisation of the sample, the semi-manufactured goods was calcined in a muffle furnace for three hours at a fixed temperature.

The resulting composite nano-photocatalyst is abbreviated as x-CeNT@Oys-y, where x denotes the Ce doping molar ratio (%), and y denotes the calcination temperature (°C). In addition, Single N-doped (N-TiO$_2$@Oys), Single Ce-dope (Ce-TiO$_2$@Oys), catalysts unloaded with modified oyster shell powder and pure TiO$_2$, were all prepared uniformly using the above procedure.

2.4 Sample characteristics

The crystal phase composition and crystallinity of composites with different calcination temperatures were analyzed by analyzing the data of powder X-ray diffraction (Rigaku, Cu Kα) 2θ range between 20° to 80°. The samples morphology tests were carried out by scanning electron microscope and specific surface area and pore size distribution measurements were carried out by a surface area and porosity analyser (QUANTACHROME, United States). The existence state of elements is analyzed and studied by a Thermo Scientific Escalab 250Xi X-ray photoelectron spectroscopy (XPS), which the source gun type was Al Kα and the test spot area was 500 μm. The surface functional groups of the photocatalysts were determined and analysed by FTIR spectra and Raman spectra. To determine the optical properties of the samples, absorption spectra in the wavelength range 200 nm–800 nm were determined using UV-vis Diffuse reflectance spectra (Hitachi, Japan) for different cerium doping amount. The measurements of the amperometric i-t curves were performed on an electrochemical workstation (CHI660E, CH Instruments, Austin, United States) where the photocurrent light source was provided by a xenon lamp with the cut-off filter.

The liquid chromatography-mass spectrometer (LC-MS) was used for the qualitative analysis of glyphosate and Aminomethyl phosphonic acid (SN/T 1923–2007). In a typical procedure, glyphosate samples were derivatised using FMOC-Cl acetonitrile solution, pH adjusted with borate buffer and methanol was added to obtain HPLC injection conditions. The final degradation products NH_4^+-N and PO_4^{3-} were determined spectrophotometrically using a nano reagent (HJ 535–2009) and a molybdenum antimony anti-spectrophotometric method (GB 11893–89) to analyse the presumed photodegradation steps of glyphosate.

2.5 Measurement of photoactivity

To investigate the photocatalytic activity of the CeNT@Oys photocatalyst, the photocatalytic degradation of PMG in aqueous solution was carried out under the irradiation of the CEL-S500 simulated sunlight xenon lamp (CEAuLight Ltd.). The aqueous solution of glyphosate (50 mg/L) was first sonicated with 100 mg photocatalyst for 15 min, the mixture was magnetically stirred in the darkroom to reach adsorption-desorption equilibrium and then
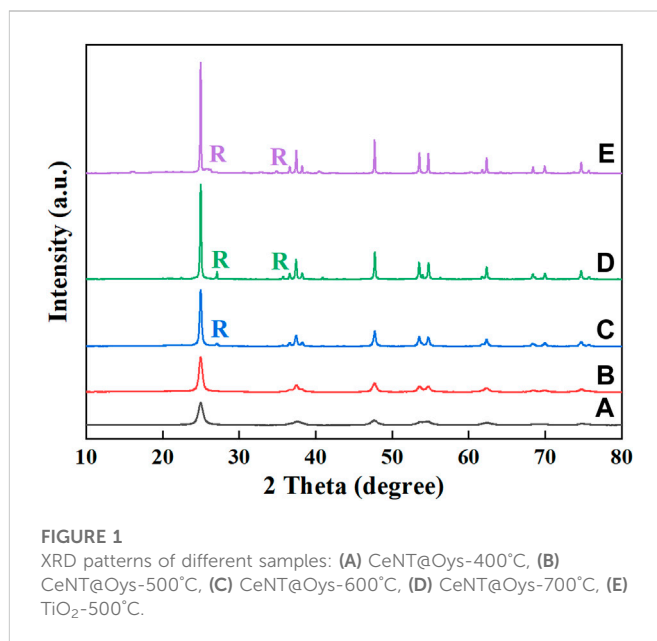
FIGURE 1
XRD patterns of different samples: **(A)** CeNT@Oys-400°C, **(B)** CeNT@Oys-500°C, **(C)** CeNT@Oys-600°C, **(D)** CeNT@Oys-700°C, **(E)** TiO$_2$-500°C.

the xenon light source was switched on. The phosphate content was determined based on the molybdenum antimony anti spectrophotometry by UV-vis (Shimadzu, UV-1800). The degradation efficiency of organic phosphorus in glyphosate was calculated according to the equation C_t/C_0, and the degradation efficiency of PMG was obtained indirectly from the inorganic phosphorus conversion rate. Where C_t is the phosphate content of the aqueous solution of PMG at moment t and C_0 is the total phosphorus content of PMG at the initial moment.

3 Results and discussion

3.1 Physicochemical properties of photocatalysts

Figure 1 shows the TiO$_2$-500°C and CeNT@Oys-y photocatalysts at different calcination temperatures, all samples have more distinctive characteristic diffraction peaks at 2θ are 25.26, 37.74, 48.00, 53.84, 55.02, and 62.64, corresponding to anatase TiO$_2$ (101), (004), (200), (105), (211) and (204) crystalline peaks, respectively (JCPSD No. 21–1,272).

As the calcination temperature increased, the diffraction peaks of CeNT@Oys composite nano-photocatalyst are sharper and more crystalline, with the rutile phase appearing at 600°C. However, no CeO$_2$ crystalline phase was found in all samples, probably because the Ce doping concentration is too low to reach the low limit of XRD detection. In addition, calcined at 500°C, the rutile phase is almost absent from the diffraction peaks of CeNT@Oys, but is present in TiO$_2$. This suggest that the doping of cerium and nitrogen inhibits the transformation of the anatase phase to the rutile phase (Tang et al., 2018). As the Ce ionic radious (Ce^{3+} = 0.111 nm, Ce^{4+} = 0.101 nm) are much larger than those of Ti^{4+} (0.068 nm), therefore, theoretically, the Ce^{3+}/Ce^{4+} is difficult to change the lattice structure of TiO$_2$, and can only be dispersed on the crystal surface or doped in the interstices (Matějová et al., 2014).
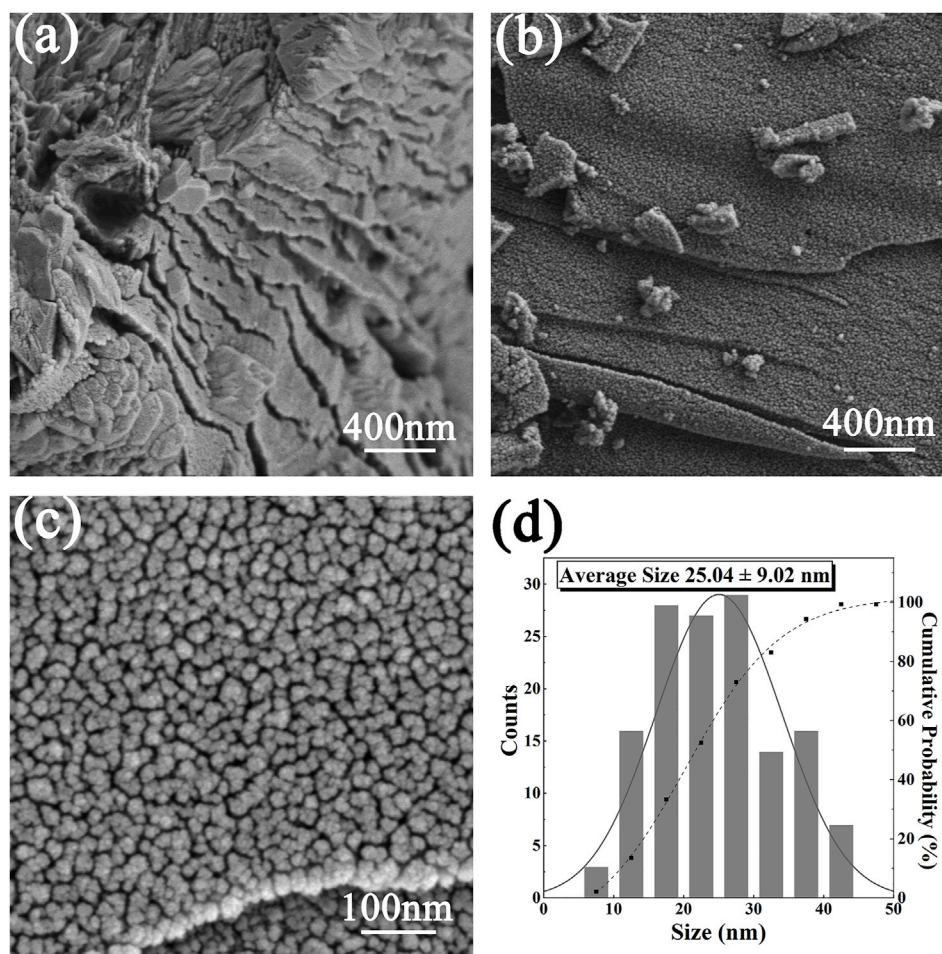
FIGURE 2
SEM micrographs of different samples: Modified oyster shell powder **(A)**, CeNT@Oys with different magnification **(B, C)**; particles analysis for Ce-N-TiO$_2$ **(D)** [done by ImageJ (v 1.52) software].

Supplementary Table S1 lists the lattice parameters, the full width at half maxima (FWHM) and crystal type for all samples, and calculates the average grain diameter based on the FWHM of main diffraction peak (101) the full width at half maxima (FWHM) based on Debye–Scherrer's equation (Tu et al., 2021). Firstly, it is observed that the increase of calcination temperature, the grain size increases with decreasing FWHM, which is mainly caused by the densification of the material due to the high surface energy of the sample particles. Secondly, Comparing TiO$_2$-500°C and CeNT@Oys-500°C, it can be seen that the doping of Ce and N leads to the reduction of grain size. It has been reported that Ce and N doping can also effectively inhibit the phase transformation of TiO$_2$. The occurrence of grain boundary segregation by cerium ions doping can inhibit microcrystal growth (Singaram et al., 2017), while N doping directly leads to the reduction of Ti-O bonding and the disruption of rutile phase structural connections, thus inhibiting them growth, which is also responsible for the reduction of grain size. In addition, the lattice parameters a and b decrease slightly with increasing temperature, while c increases more significantly. Unfortunately, no significant crystalline phases are detected due to the low doping of the modified oyster shell powder. Supplementary Figure S1 plots the XRD peaks of the modified oyster shell powder, whose XRD spectrum is dominated by the diffraction peaks of Ca (OH)$_2$ and CaCO$_3$.

Figures 2A–C shows SEM micrographs of different samples. The modified oyster shell powder shows a layered plate-like microstructure. Figure 2B shows that the Ce-N-TiO$_2$ nanoparticles are uniformly distributed on the surface of the modified oyster shell powder, and there is some aggregation phenomenon. After magnification, the Ce-N-TiO$_2$ nanoparticles show a uniform particle size. The average particle size of 25.04 nm ± 9.02 nm was obtained from the statistical analysis of the particles in Figure 2D, which is slightly higher compared to the XRD calculation results because the Scherrer formula only imputes the particle size of scattered particles, while the presence of aggregation behaviour of particles in photographs taken by scanning electron microscopy was counted by computer.

Figure 3 shows the N$_2$ adsorption-desorption isothermal curves and the inserted image shows the pore size distribution plot. According to the IUPAC classification analysis, both Ce-N-TiO$_2$ and CeNT@Oys have type IV isothermal adsorption curves and there is an adsorption hysteresis in the relative pressure range of approximately 0.6–0.9 for P/P$_0$ and the presence of an H$_2$-type hysteresis loop, indicating the presence of a mesoporous structure (Shaari et al., 2012), which often
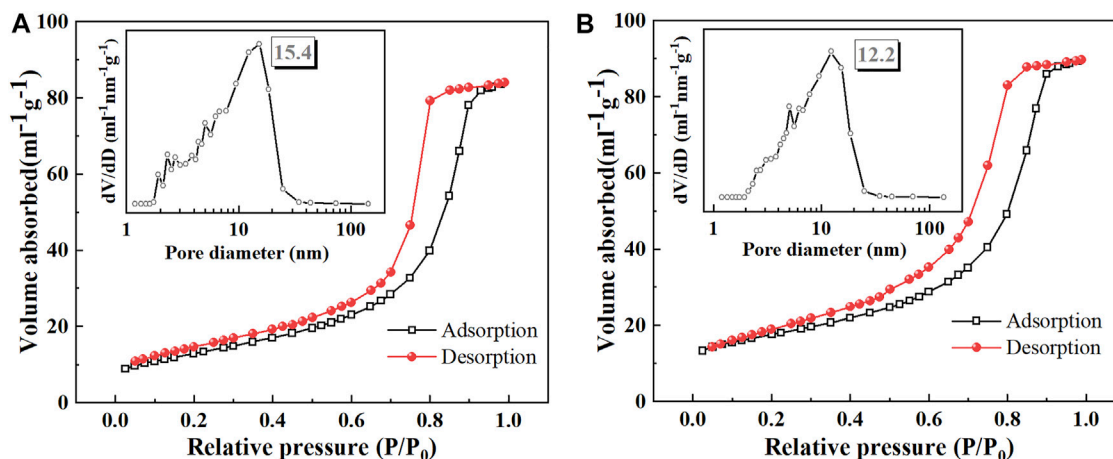
FIGURE 3
N_2 adsorption-desorption isothermal curves of Ce-N-TiO$_2$ **(A)** and CeNT@Oys **(B)**. (inset: The pore size distribution curve of **(A)** Ce-N-TiO$_2$ and **(B)** CeNT@Oys).
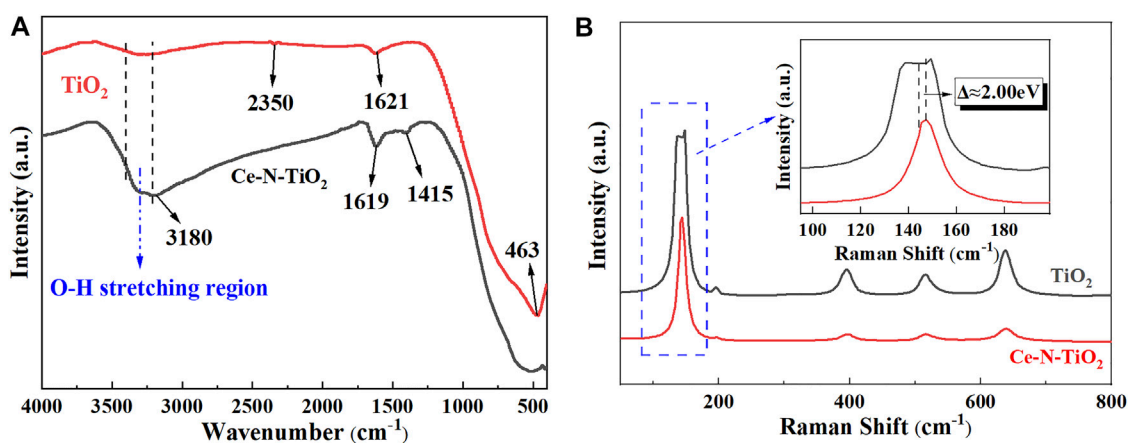

FIGURE 4
FTIR spectra **(A)** and Raman spectra **(B)** of TiO$_2$ and 0.5%-Ce-N-TiO$_2$.

appears in the interstitial pore structure of dense spherical particles. The adsorption saturation platform is observed in the curve when the relative pressure is greater than 0.9, indicating that the pore size distribution of the sample is uniform. The specific surface area of Ce-N-TiO$_2$ before and after doping with modified oyster powder is 61.649 m²/g and 75.301 m²/g, respectively, indicating that to a certain extent the doping of modified oyster powder increased the specific surface area of Ce-N-TiO$_2$. The XRD characterization results show that the doping of Ce and N leads to the reduction of TiO$_2$ grain size, thereby increasing the active sites of the catalyst. Based on the Barret-Joyner-Halenda method, the pore size distribution was estimated from the adsorption branch of the nitrogen isotherm, which favourably demonstrated that most of the sample pores were mesoporous structures with average pore centres of 15.4 nm and 12.2 nm, respectively.

Figure 4A shows the infrared spectrogram of TiO$_2$ and CeNT@Oys. One of the most pronounced absorption peaks is located in the

460 cm⁻¹–520 cm⁻¹ range, which is mainly attributed to the stretching vibration of the Ti-O bond. The wider and weaker peaks and valleys of the co-doped catalysts may be caused by the doping of the metal Ce affecting the Ti-O bond formation. The presence of a Ce-Ti-O bond at around 600 cm⁻¹ has been reported (Maarisetty and Baral 2019), but no distinctive peak appears due to the low Ce doping in this experiment, although the broadening of the trough at this point also demonstrates the presence of a Ce-Ti-O bond. The peak at 1,620 cm⁻¹ and the broad peak within 3,200 cm⁻¹–3,400 cm⁻¹ represent the bending vibration and stretching vibration of water molecules physically or chemically adsorbed on the surface and hydroxyl groups at different active sites, respectively. Further, The intensity of the co-doped absorption peak is significantly higher than that of the pure sample, indicating that it absorbs more hydroxyl groups on the surface, which is conducive to the photocatalytic reaction. The peak at 1,420 cm⁻¹ and the broad peak at 3,180 cm⁻¹ are attributed to the bending vibration and stretching vibration of the
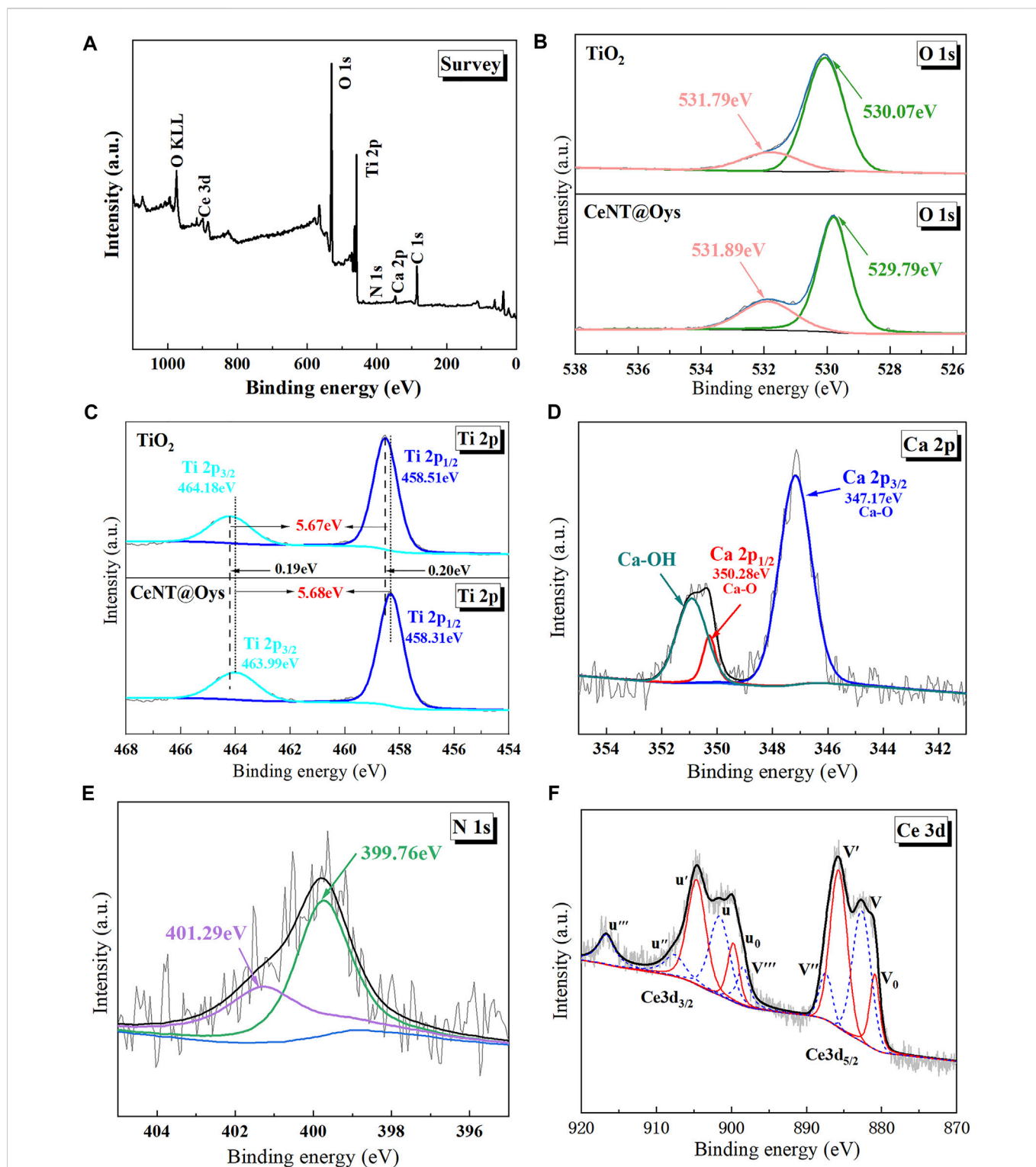
FIGURE 5
XPS spectrum of the CeNT@Oys composite nano-photocatalyst **(A)**; high resolution XPS spectra of Ti 2p **(B)**; O 1s **(C)**; Ca 2p **(D)**; N 1s **(E)**; Ce 3d **(F)**.

N-H bond. The weak peak at 2,350 cm^{-1} in the spectrum of the pure sample is a characteristic CO_2 absorption peak due to the incomplete evaporation of the ethanol solvent during preparation (He et al., 2021).

Raman spectroscopy was used to further study the changes of molecular vibration after modification. The Raman activity mode of anatase TiO_2 is $(A_1+2B_1+3E_g)$ (Nasir et al., 2014), and Figure 4B shows that both samples have significant vibrational peaks at about 145 cm^{-1} (E_g), 196 cm^{-1} (E_g), 396 cm^{-1} (B_1), 514 cm^{-1} (A_1+B_1) and 638 cm^{-1} (E_g). The peaks at 395.56 cm^{-1} and 514.92 cm^{-1} represent the stretching vibrations of the O-Ti-O bond, and the peaks of 145 cm^{-1} and 638 cm^{-1} can be attributed to the bending vibrations of this bond.

It has been reported (Choudhury et al., 2013) that the main reason for the variation in peak height, width and position of the Raman spectra is the different size and defects of the nanoparticles. The Raman vibrational peak intensity was significantly reduced and the peak width became larger due to the doping of Ce and N. The peak of 196 cm^{-1} position of the co-doped sample was shifted to a higher wave number as can be seen from Figure 4B, and the occurrence of this phenomenon can be attributed to the following two points. Dhanalakshmi et al. (2017) analysed that the shift of the peak of 196 cm^{-1} to higher wave numbers is due to the presence of oxygen vacancies. Therefore, the ionic radii of Ce and Ti are different and when Ce is doped in the lattice gap it may causes oxygen vacancy defects leading to lattice distortion. Secondly, The formation of O-Ti-N bond by N doping leads to the decrease of Ti-O bond strength and the change of vibration peak intensity and width. In addition, XRD analysis shows that co-doping leads to a reduction in the particle size of the sample, which also causes a change in the vibrational peak.

X-ray photoelectron spectroscopy was used to determine the surface chemical composition and binding state of the sample. The full spectrum of the CeNT@Oys catalyst is shown in Figure 5A, indicating that the sample contains the elements Ti, O, C, Ca, N and Ce, with Ti and O being the dominant elements in the sample, while C may be residual carbon due to incomplete evaporation of the preparation reagent anhydrous ethanol and carbon-based contamination of the XPS detection equipment (Matějová et al., 2014; He et al., 2021).

Figures 5B–F show the high-resolution spectra based on the XPS Peak41 software split-peak fit with charge correction for the C 1s main peak binding energy (284.80 eV). Figure 5B shows that the O 1s are deconvoluted into a double peak, with the characteristic peaks (529.79eV, 530.07eV) representing lattice oxygen (O-Ti-O) and an additional peak (531.79eV, 531.89eV) attributed to the presence of chemisorbed oxygen or hydroxyl groups. Notably, the peak at 531.89eV for the composite nano-photocatalyst is higher than that of pure TiO_2, indicating more hydroxyl groups and adsorbed oxygen on the surface of the sample after co-doping, which undoubtedly facilitates the photoinduced electron-hole pairs transfer and optimises the photocatalytic performance. Figure 5C shows the Ti 2p high-resolution spectrum, with a difference of 5.6eV between the double peaks consistent with Ti^{4+} of anatase TiO_2, indicating that Ti is only present in the form of Ti^{4+}, and there is no Ti^{3+}. It is not difficult to find that the peak positions of Ti 2p and O 1s are both shifted towards the lower binding energy by 0.2 eV, which is mainly due to the electronegativity of N being less than that of O (Wang Y. et al., 2011b), and the N doping leads to an increase in the electron cloud density around Ti and O, which reduces the binding energy, and the peak positions will then shift negatively.

Figure 5D shows the Ca 2p high-resolution spectrum. After fitting the split peaks, the presence of a Ca-O bond at 347.16 eV in Ca $2p_{3/2}$, a Ca-O bond at 350.63 eV and a Ca-OH bond at 351.22 eV in Ca $2p_{1/2}$ indicates that the presence of the modified oyster shell powder profits the adsorption of hydroxyl groups.

Previous studies have shown that there are slight differences regarding the analysis of N 1s energy spectra in N-TiO_2. Most researchers believe that the N 1s binding energy is mainly related to the N in TiO_2 doping form or the N-TiO_2 synthesis method (Senthilnathan and Philip 2010). The TiN characteristic peak is near 396 eV, and the characteristic peak at 396 eV–398 eV is attributed to the O-Ti-N bond or N-Ti-N bond formed by the
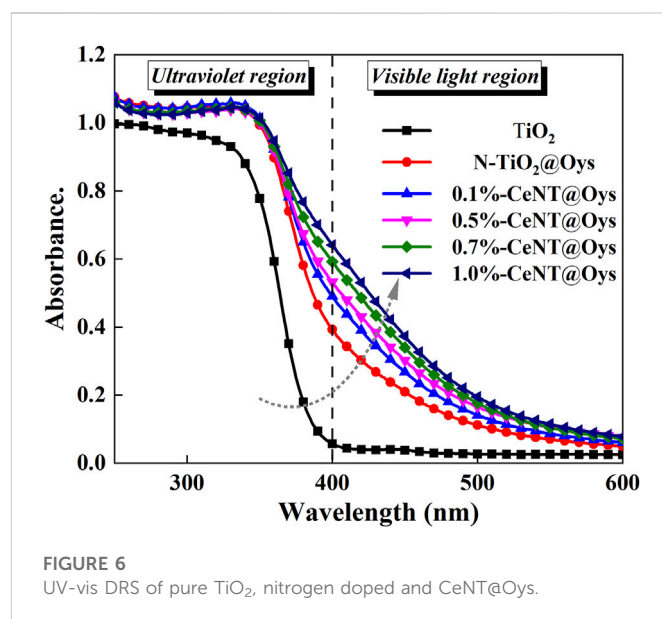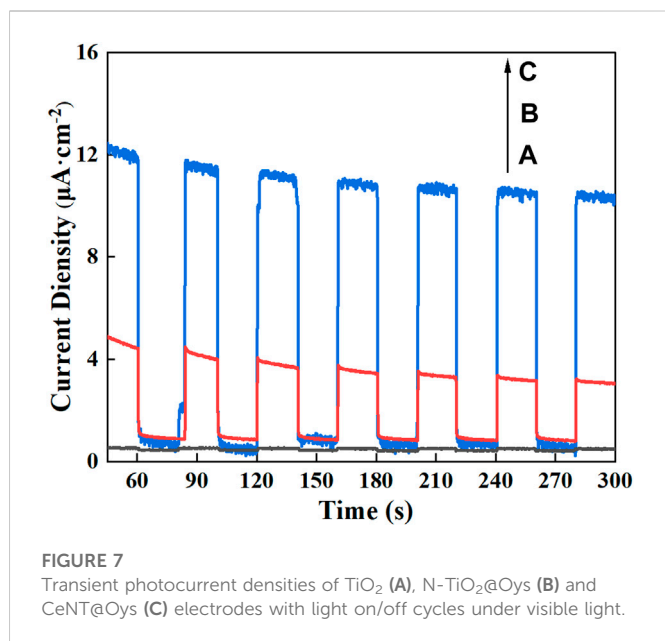

FIGURE 6
UV-vis DRS of pure TiO_2, nitrogen doped and CeNT@Oys.

replacement of lattice oxygen by nitrogen species, and the characteristic peak at 398 eV–401 eV is attributed to the interstitial N species. In this studies, no N 1s peak for Ti-N was detected in the N1s fitted curve at 396 eV–398 eV, and no TiN (111) and (220) diffraction peaks were detected in XRD (Lee et al., 2013). It is clear that the peak at 399.76 eV is formed by te structural features of N in the interstitial form forming Ti-N-O or N-O-Ti. Similarly, 401.29 eV may be associated with the presence of N-H bonds (Chen and Liu 2017; Bian et al., 2021).

Figure 5F shows an XPS diagram of the Ce3d split-peak fit. Due to the different hybridisation of the Ce 4f and O 2p orbitals and the different electronic valence states of Ce^{3+} and Ce^{4+}, the Ce 3d spectrum splits the $3d_{5/2}$ spin-orbit state labeled v and the $3d_{3/2}$ spin-orbit state labeled u. The inverse fold product was performed according to the rules constructed by Burroughs et al. (1976). The red solid fitted peaks represent Ce^{4+} and the blue dashed fitted peaks represent Ce^{3+}. Taking Ce $3d_{5/2}$ as an example, v, v" and v'" are the characteristic peaks representing Ce^{4+} in the $3d_{5/2}$ electronic levels, where v and v'" are attributed to the allocation of two or one electron from the O 2p orbital to the Ce 4f orbital, forming the $(5d6s)^0 4f^2$ O $2p^4$ and $(5d6s)^0 4f^1$ O $2p^5$ hybrid configurations. v'" is caused by the primary photoelectric emission of Ce^{4+} (Xu et al., 2006), forming the $(5d6s)^0 4f^0$ O $2p^6$ electronic configuration. v_0 and v' are the $3d_{5/2}$ electronic levels that construct the characteristic Ce^{3+} peak. Where v' represents the $(5d6s)^0 4f^1$ O $2p^6$ unhybridised configuration, and v_0 represents $(5d6s)^0 4f^2$ O $2p^5$. It is inferred that Ce^{3+} and Ce^{4+} are present in the catalyst samples, combined with XRD analysis results it is clear that Ce can only be present in the grain boundary gaps or on the surface, forming a Ce-O-Ti bond structure.

The optical properties of the x%-CeNT@Oys catalysts were characterized by UV-vis diffuse reflectance spectrum. As shown in Figure 6, TiO_2 exhibit high absorbance in the UV region due to the photoexcited carrier leap in the anatase band gap and no absorbance in the visible region. In contrast, the co-doped samples show significantly enhanced light absorption in the UV and visible regions, and the significant red-shift of CeNT@Oys compared to TiO_2 is mainly attributed to the reduction in its forbidden band width.

FIGURE 7
Transient photocurrent densities of TiO$_2$ **(A)**, N-TiO$_2$@Oys **(B)** and CeNT@Oys **(C)** electrodes with light on/off cycles under visible light.

Firstly, Ce doping forms the Ce 4f impurity level below the Ti 3d minimum in the TiO$_2$ conduction band, thus reducing the forbidden band width (Xu et al., 2002), and the different electronic structure of Ce^{4+}(4f^{0}5d^0)/Ce^{3+}(4f^{1}5d^0) results in a better electron-hole separation. The redshift effect at the absorption edge becomes more and more pronounced with increasing Ce doping, unfortunately, it was shown (Ikeda et al., 2001) that when Ce doping exceeds a certain amount, it may not improve the photocatalyst degradation activity even if the redshift is more pronounced leading to a smaller band gap. Secondly, N doping forms an N 2p impurity energy level above the O 2p in the TiO$_2$ valence band (Barolo et al., 2012), and ultimately the co-doped sample significantly reduces the band gap energy and improves the photocatalytic performance with the synergistic effect of both. Ce and N doping not only allows the sample to make full use of visible light energy, but also facilitates the improvement of photogenerated electron-hole pair separation efficiency.

Based on the Kubelka-Muna equation F(R)=(1-R)^2/2R (Spadavecchia et al., 2010; López and Gómez 2011), the absorption function was calculated from the reflectance data and the curve was plotted with hv as the horizontal coordinate and [F(R) • E]$^{1/2}$ as the vertical coordinate as shown in the Supplementary Figure S2. The band gap energies of TiO$_2$, N-TiO$_2$@Oys, 0.5%-CeNT@Oys and 1.0%-CeNT@Oys samples are 3.20 eV, 3.00 eV, 2.91 eV, and 2.69 eV, corresponding to absorption edges of 387 nm, 413 nm, 426 nm, and 461 nm, respectively.

The photogenerated carrier separation properties of the samples were analysed by comparing the photocurrent tests before and after TiO$_2$ doping with ions, with the usual photocurrent intensity representing the separation efficiency of the electron-hole pairs. Figure 7 records the instantaneous photocurrent response when switching the xenon lamp on and off five times. The photocurrent response signal of N-TiO$_2$@Oys is enhanced by a factor of 16.5 compared to TiO$_2$, and again by a factor of about 4 after continued doping with Ce. The introduction of N 2p hybridisation orbitals by N doping. Ulteriorly, Ce^{3+}/Ce^{4+} is known as the "oxygen tank" due to its special redox properties (Chaker et al., 2020), Ce^{4+} has

a strong electron capture ability to improve the separation efficiency of electron-hole pairs, while Ce^{3+} can absorb oxygen to form superoxide radicals to participate in photocatalytic reactions. It is well established that the appropriate amount of Ce and N doping can effectively improve the separation efficiency of photogenerated carriers.

3.2 Photocatalytic oxidation of PMG

3.2.1 Screening of catalysts and kinetic study of PMG

To evaluate the photocatalytic degradation activity of the prepared series of nano-materials on glyphosate, an aqueous solution of 50 mg/L PMG was degraded under simulated sunlight xenon lamp. Figure 8A shows the effect of calcination at different temperatures for the degradation of PMG by 0.5%-CeNT@Oys-y°C. Glyphosate degradation reached over 80% at 500°C, however, it dropped to 40% at 700°C. The reason for the low degradation of glyphosate is that TiO$_2$ does not reach the crystallization critical temperature of amorphous phase-anatase, forming a crystalline phase TiO$_2$ with low crystallinity at lower calcination temperature. Moreover, the higher the calcination temperature the larger the catalyst particle size was calculated from the XRD characterization data by the Scheler formula, indicating that agglomeration and sintering on the catalyst surface intensified during the high temperature calcination process, resulting in a lower specific surface area of the sample (Suwannaruang et al., 2018). In addition, the loss of nitrogen or cerium doping at high calcination temperatures may affect the effective formation of impurity energy levels (Wang C. et al., 2011). Therefore, the subsequent experiments were carried out at 500°C.

Blank control experiments were first carried out, where the degradation efficiency was determined to be less than 5% for the aqueous glyphosate solution irradiated in the absence of catalyst, the degradation of glyphosate without catalyst is ignored. The results of the comparative experiments are shown in Figure 8B, and the specific parameters are shown in Supplementary Table S2. All of the modified catalysts show higher degradation efficiency compared to Pure TiO$_2$, due to the fact that TiO$_2$ has a wider forbidden band and only absorbs 4% of the UV light resulting in a much lower photo response than the other five samples under simulated sunlight. Analysis of the UV-vis DRS characterization results show that the introduction of impurity energy levels by N and Ce doping lead to a significant increase in the absorption of light sources in the visible wavelength range, resulting in a red-shift of the absorption edge and hence more photogenerated carriers to improve the degradation efficiency, which also indicates that the prepared catalysts already have visible light responsive activity. In comparison with 0.1%-CeNT and 0.1%-CeNT@Oys, the latter has a higher photodegradation capacity, which is mainly attributed to the increase of adsorption sites on the surface of the catalyst and enhancement of adsorption capacity due to the doping of modified oyster shell powder.

Furthermore, we observed that the degradation efficiency of the different Ce doping samples were in the order of 1.0%-CeNT@Oys<0.1%-CeNT@Oys<0.5%-CeNT@Oys, and 1.0%-CeNT@Oys was not even as high as that of the undoped Ce samples. This result indicates that there is an optimum value of Ce doping for photocatalytic degradation activity in the research scope, and validates the standpoint that even the band gap of photocatalyst is narrower, it cannot fully explain the view that photocatalyst has stronger ability to degrade pollutants.
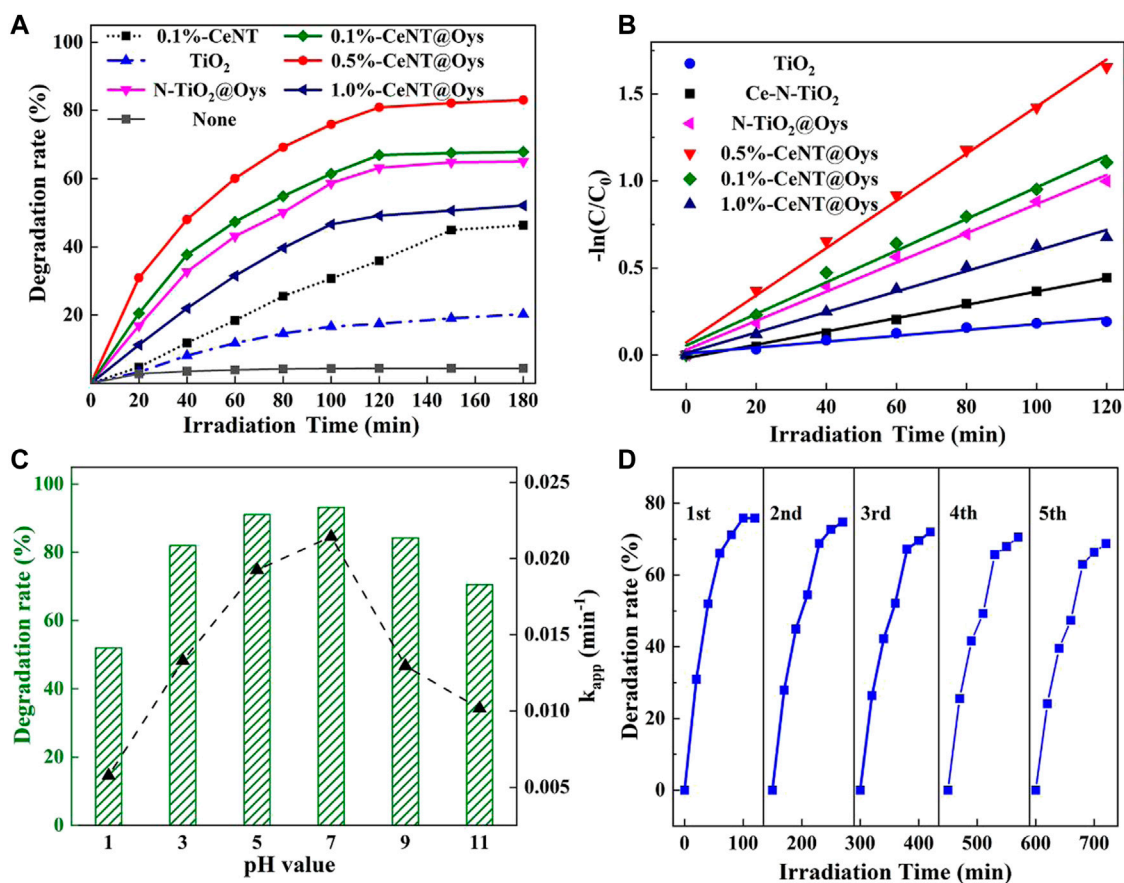
FIGURE 8
(A) Photodegradation efficiency of PMG under visible light irradiation using various types of catalyst samples; **(B)** kinetic profiles of PMG degradation results using various types of catalyst samples; **(C)** effect of initial pH on PMG degradation; **(D)** the reusability experiment results of 0.5%-CeNT@Oys-500°C.

We make the following explanations for the above phenomena. There is no doubt that the visible light degradation activity is increased when the appropriate amount of Ce is doped into TiO_2 (Xu et al., 2006), due to the introduction of Ce 4f impurity energy level by the doping of Ce ions to reduce the TiO_2 forbidden band width and increase its ability to absorb visible light. However, it has been shown (Xiao et al., 2006) that the amount of lanthanide doping is inversely proportional to the thickness of the space charge layer. When the doping rate of Ce is too high, the depth of light shooting in the catalyst far exceeds the thickness of the space charge layer at the photocatalyst-organic molecule interface, and the charge carrier complexation rate will increase, which will lead to the deterioration of the photocatalyst activity. Interestingly, some studies (Liu et al., 2008) have shown that excessive Ce doping will lead to the formation of CeO_2 microcrystals in TiO_2 surface, which can further increase the catalyst photoactivity, and this deserves further investigation.

According to the Langmuir–Hinshelwood (L-H) mechanism (Hoffman and Ronald 1995), the degradation of PMG is consistent with an apparent first-order kinetic model over 120 min. Based on the above model, we determined the PMG photodegradation rate by the equation $-\ln(C_t/C_0) = k_{app}t$. Where the k_{app} represents the apparent reaction rate constant, t is the time of light exposure, C_0 represents the initial concentration of total phosphorus in the PMG solution and C_t represents the concentration of organic phosphorus remaining in the

PMG solution at time t. The calculated results indicate that the combination of Ce, N co-doping and modified oyster shell powder produced significant adsorption-photocatalytic synergy under simulated sunlight xenon light, with the apparent rate constant for PMG degradation kinetics of 0.5%-CeNT@Oys being about 8.0 times higher than that of pure TiO_2.

3.2.2 Effect of solution pH

Figure 8C shows the degradation efficiency and apparent rate constants of 50 mg/L glyphosate at different initial pH values. The different pH value adjustments were achieved by the dropwise addition of 0.1 M HCl and 0.1 M NaOH. As the pH value increased from 1.0 to 7.0, the glyphosate degradation efficiency and k_{app} increased from 52% to 0.576×10^{-2} min^{-1}–91.05% and 2.142×10^{-2} min^{-1}, respectively, however, when the pH value increased from 7.0 to 11.0, the glyphosate degradation efficiency and k_{app} decreased instead to 70.53% and 1.017×10^{-2} min^{-1}.

The main reasons for the variation in glyphosate degradation efficiency at different initial pH values were explained by the surface zeta potential of the synthesis catalysts and the morphological distribution of glyphosate at different pH values (Aba-Guevara et al., 2017). The zeta potentials of Pure TiO_2 and CeNT@Oys catalysts at different pH were determined by zeta potential meter and the null point potential (pH$_{pzc}$) was measured. As shown in

Supplementary Figure S3 that the pH_{pzc} of CeNT@Oys is 7.07. When the pH of glyphosate solution is greater than 7.07, the surface of the sample is negatively charged, Otherwise, the surface carries a positive charge. To ensure the accuracy of the test, the pH_{pzc} of pure TiO_2 catalyst is compared to 5.72. In a previous study, the pKa of PMG was 2.22, 5.44 and 10.13, respectively (Sheals et al., 2002). When pH < 2.22, glyphosate mainly exists in aqueous solution in an electrically neutral state (H_3PMG), and in the range 2.22 < pH < 5.44, glyphosate mostly exists in the form of H_2PMG^{1-} with a negative charge by dehydrogenation from the carboxylic acid group. When 5.44 < pH < 10.13, most glyphosate continues to dehydrogenation at the phosphate group to form $HPMG^{2-}$ with two negative charges in solution; at pH > 10.13 it exists as PMG^{3-} with dehydrogenation from the amino group.

According to Coulomb's law, the negative charge on the surface of glyphosate and the positive charge on the catalyst surface generate electrostatic attraction when the pH is in the range of 2.22–7.07, which is easy to make the active group contact glyphosate molecule and play a role on it. While in the range of pH > 7.07, there is electrostatic mutual repulsion between the two, which leads to the decline of the adsorption performance of the catalyst, thus it is difficult for the active groups to approach and attack glyphosate molecules. Therefore, the highest degradation efficiency of glyphosate at pH 7 is mainly due to the synergistic effect of adsorption-photocatalysis. The low degradation efficiency at the initial pH 1 of the glyphosate solution may be due to the reaction of excess hydrion and hydroxide radicals in the presence of extreme acidity, which depletes the active groups. In the pH range of 3–7, the gradual increase of glyphosate degradation efficiency can be explained by the fact that the degree of mutual attraction between the two increases with the increase of glyphosate surface negative charge. Moreover, some studies (Rajoriya et al., 2019) have proved that glyphosate is more stable and difficult to degrade under high acid conditions, and photogenerated electrons will be captured by too many hydrogen ions.

3.2.3 Stability of photocatalyst

Reusability is always one of the most important parameters in the practical application of photocatalysts. After the previous round of degradation test the samples were filtered several times with distilled water and vacuum drying at 60°C. The same degradation tests were then repeated five times, and Figure 8D shows the test results of five cycles of 720 min photocatalytic degradation. From the first round to the last round, the degradation efficiency of glyphosate decreased from 75.88% to 68.79%, but not significantly. The decrease in removal rate may be due to artificially caused weight loss during the recycling process after catalyst use or incomplete washing of residues on the catalyst surface. Therefore, we conclude that the CeNT@Oys photocatalyst has good stability and recyclability in degrading glyphosate.

3.3 Photocatalytic degradation mechanism

In order to determine the active species acting in the photocatalytic reaction of CeNT@Oys composite nano-photocatalyst, quenching experiments were carried out under optimal reaction conditions, in which the addition of a certain amount of isopropyl alcohol (IPA), disodium ethylenediaminetetraacetate (EDTA-2Na) and p-benzoquinone

(BQ) were used as chemical reagents to capture $\bullet$ OH, vacancies (h^+) and $\bullet$ O_2^-, respectively. The experimental results are shown in Figure 9A. The addition of EDTA-2Na severely affected the degradation efficiency of glyphosate, indicating that Holes or other active groups formed by reacting with holes are the main reactive species for glyphosate degradation. The addition of BQ and IPA also reduced the degradation efficiency of glyphosate by 27.9% and 14.48%, respectively. This phenomenon caused by the decrease in hole consumption and increase in electron-hole complex rate after the quenching of superoxide and hydroxyl radicals, and also indicates that both superoxide and hydroxyl radicals play an oxidative role in the degradation of glyphosate.

The electron paramagnetic resonance test using dimethyl pyridine N-oxide as a trapping agent was used to further demonstrate the presence of $\bullet$ OH and $\bullet$ O_2^- in the reaction system, as shown in Figures 9B, C. We found that there was no clear characteristic signal in the dark environment, however, However, with the irradiation of visible light, the characteristic signal of DMPO-$\bullet$ OH with a ratio of 1:2:2:1 and the characteristic signal of DMPO-$\bullet$ O_2^- with six peaks appeared obviously, and there was a good linear relationship between the increase in light reaction time and the consequent increase in radical signal intensity, indicating the presence of both radicals in the CeNT@Oys and glyphosate systems. This performance is in full agreement with the quenching experiments, further confirming that the CeNT@Oys composite nano-photocatalyst can effectively promote the formation of $\bullet$ OH and $\bullet$ O_2^-.

Through the above series of material property characterization and quenching experiments and the EPR test, a reasonable analysis of the adsorption-photocatalytic degradation mechanism of CeNT@Oys composite nano-photocatalyst for glyphosate degradation in simulated sunlight is proposed as shown in Figure 10.

From XRD, XPS and other characterization, it can be seen that N is doped into TiO_2 in interstitial form, while Ce mostly stays on the lattice surface, with a few Ce entering the TiO_2 lattice in interstitial form. Combined with UV-vis DRS testing, it can be seen that N 2p orbitals are doped directly above the TiO_2 valence band and Ce 4f orbitals directly below the conduction band, as well as a small amount of Ce^{4+} oxide loaded on the surface of TiO_2.

Firstly, glyphosate molecules are adsorbed onto the photocatalysts surface and the adsorption phase was in accordance with a quasi-secondary kinetic model (Zhang et al., 2022), which can be divided into three phases: external liquid film diffusion dominated, intraparticle or pore diffusion and an adsorption equilibrium phase. Photocatalysis then proceeds. Since the doping of Ce and N excites the catalyst to act at visible wavelengths, the electron leap in the degradation of glyphosate by CeNT@Oys is mainly through 1) O 2p CB → Ti 2p VB; 2) N 2p hybrid orbital → Ti 2p VB; 3) O 2p CB → N 2p hybrid orbital → Ti 2p VB; 4) O 2p CB → Ce 4f hybrid orbital → Ti 2p VB is achieved in four forms. The doping of Ce can effectively reduce the electron-hole complexation rate, because the photogenerated carriers are partly excited to Ce 4f hybrid orbital. In summary, under the irradiation of sunlight, h^+, $\bullet$ OH and $\bullet$ O_2^- jointly attack glyphosate molecules to break them up.

3.4 Proposed degradation routes of PMG

As Supplementary Figure S4 shows the bond breaking mode of glyphosate degradation, but after analysis in this experiment mainly
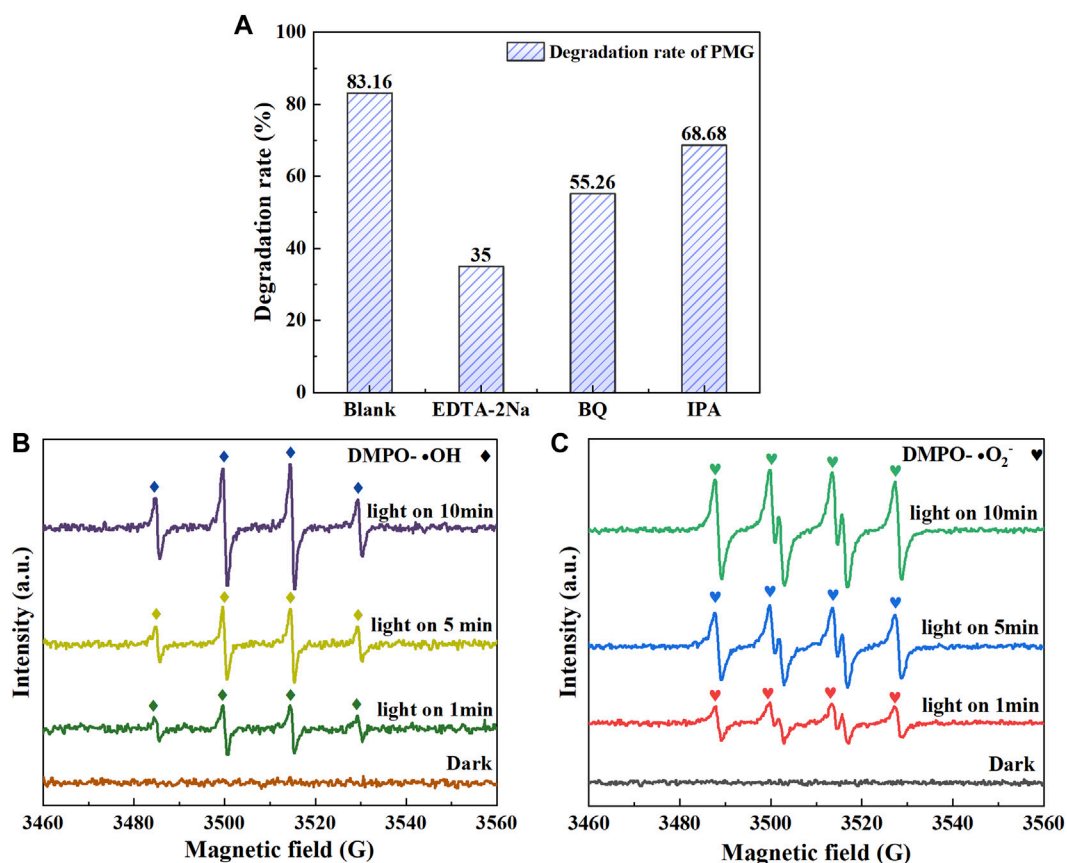
FIGURE 9
Effects of different scavengers on photocatalytic degradation of PMG **(A)**; EPR spectra recorded in the dark and visible light with 1min, 5min and 10 min of 0.5%-CeNT@TiO$_2$ photocatalyst **(B)** and **(C)**.
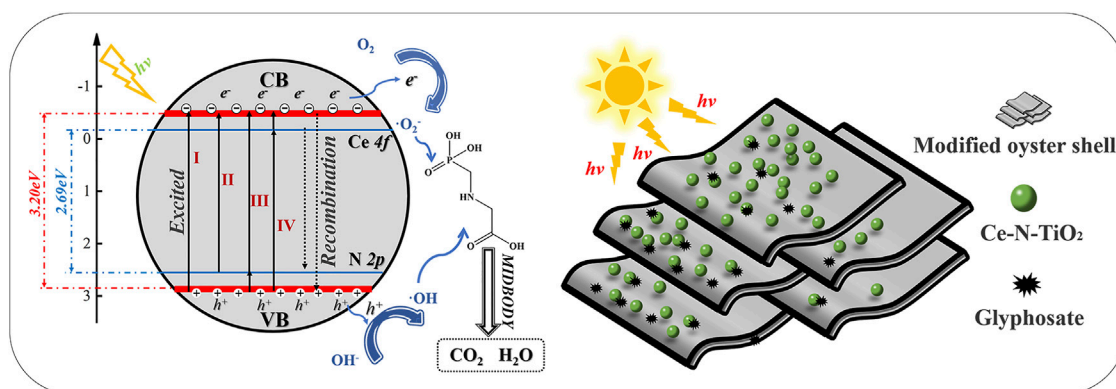

FIGURE 10
Proposed visible-light photocatalytic glyphosate mechanism by the CeNT@Oys.

C-N bond breaking was the main focus. In conjunction with SN/T 1923–200 Appendix A, as can be seen in Supplementary Figure S5A, the relative molecular mass of the glyphosate derivative is 391 and the presence of a cation peak at m/z 392 ([M + H]$^+$) is clearly representative of the presence of the glyphosate molecule and the presence of fragment ion peaks at m/z 213.95 ([M-C$_{14}$H$_{10}$ + H]$^+$) and

m/z 88.04 ([C$_3$H$_8$NO$_5$P-H$_3$PO$_3$+H]$^+$) in the full scan mass spectra of the daughter ions. For Supplementary Figure S5B, it can be seen that after photodegradation of glyphosate to small molecules, the main AMPA derivative has an ion peak at m/z 334 ([M + H]$^+$), while its fragment ion peaks at m/z 179.01 ([C$_{14}$ + H$_{10}$]$^+$) and m/z 112.06 ([CH$_6$NO$_3$+H]$^+$) are present. It was shown that the main pathways of

degradation of glyphosate in the samples were $\bullet$ OH and $\bullet$ O_2^- attacking the C-N bond of glyphosate to generate intermediates such as AMPA and acetic acid, or directly skipping acetic acid to generate AMPA and glyoxalate intermediates, for the nitrogen in AMPA, NH_4^+-N was the main mineralisation product (Negishi et al., 2012), therefore, eventually AMPA degraded to inorganic substances such as PO_4^{3-}, NH_4^+-N, H_2O and CO_2, and acetic acid or glyoxalate gradually degraded to CO_2 and H_2O. Unlike the analysis by Jaisi et al. (2016) and Echavia et al. (2009), its degradation intermediate is sarcosine, which then further breaks the bond and cleaves to aliphatic structures such as formic acid, oxalic acid and acetic acid, eventually generating inorganic substances such as phosphate and CO_2.

4 Conclusion

A simple hydrothermal synthesis using urea and cerium nitrate hexahydrate as precursors and modified oyster shell powder as the carrier was used to synthesize the Ce and N doped TiO_2 composite nano photocatalysts. The doping of modified oyster shell powder increased the specific surface area of Ce-N-TiO_2 from 61.649 m^2/g to 75.301 m^2/g. FTIR and Ramn showed that the oxygen affinity of the composite catalyst is stronger than that of TiO_2, and the surface absorbed more hydroxyl groups. Based on the peak fitting of XPS peak software, it is known that Ce exists in the form of surface adhesion or interstitial doping, while N is doped in the form of interstitial. The photon absorption capacity of the CeNT@Oys nano-photocatalysts are significantly improved, and the light absorption edges of 0.1%-CeNT@Oys, 0.5%-CeNT@Oys and 1.0%-CeNT@Oys are calculated to be red-shifted to 413 nm, 426 nm, and 461 nm. Analysis of the degradation effect of different catalysts by reaction kinetics revealed that the highest catalyst degradation efficiency was achieved at 0.5% Ce doping rate. The catalyst is recovered and reused to demonstrate good recyclability and stability. The quenching test and EPR test showed that the samples degraded glyphosate with h^+ as the predominant reactive species and $\bullet$ OH and $\bullet$ O_2^- as the secondary. The degradation pathway of glyphosate is mainly based on C-P bond and C-N bond breakage. In conclusion it shows that CeNT@Oys is a green, efficient, low-priced and recyclable photocatalyst, which has important basic theoretical significance and potential application value for safeguarding the health of the ecological environment.

Data availability statement

The original contributions presented in the study are included in the article/Supplementary Material, further inquiries can be directed to the corresponding author.

Author contributions

WZ: Validation, formal analysis, investigation, writing–original draft QY: Conceptualization, writing–review and editing, supervision, project administration, funding acquisition JS: Supervision, writing–review and editing AW: Supervision, writing–review and editing HL: Writing–review and editing XY: Writing–review and editing.

Acknowledgments

Conflict of interest

The authors declare that the research was conducted in the absence of any commercial or financial relationships that could be construed as a potential conflict of interest.

Publisher's note

All claims expressed in this article are solely those of the authors and do not necessarily represent those of their affiliated organizations, or those of the publisher, the editors and the reviewers. Any product that may be evaluated in this article, or claim that may be made by its manufacturer, is not guaranteed or endorsed by the publisher.

Supplementary material

The Supplementary Material for this article can be found online at: https://www.frontiersin.org/articles/10.3389/fenvs.2023.1131284/full#supplementary-material

References

Aba-Guevara, C. G., Medina-Ramírez, I. E., Hernández-Ramírez, A., Jáuregui-Rincón, J., Lozano-Álvarez, J. A., and Rodríguez-López, J. L. (2017). Comparison of two synthesis methods on the preparation of Fe, N-Co-doped TiO_2 materials for degradation of pharmaceutical compounds under visible light. *Ceram. Int.* 43 (6), 5068–5079. doi:10.1016/j.ceramint.2017.01.018

Abbas, M. N. (2014). Phosphorus removal from wastewater using rice husk and subsequent utilization of the waste residue. *Desalination Water Treat.* 55 (4), 970–977. doi:10.1080/19443994.2014.922494

Ali, H., Babar, H., Shah, T., Sajid, M., Qasim, M., and Javed, S. (2018). Preparation techniques of TiO_2 nanofluids and challenges: A review. *Appl. Sci.* 8 (4), 587. doi:10.3390/app8040587

Alipanahpour Dil, E., Ghaedi, M., Asfaram, A., Mehrabi, F., Bazrafshan, A. A., and Tayebi, L. (2019). Synthesis and application of Ce-doped TiO_2 nanoparticles loaded on activated carbon for ultrasound-assisted adsorption of Basic Red 46 dye. *Ultrason. Sonochem* 58, 104702. doi:10.1016/j.ultsonch.2019.104702

Alvarez-García, S., Ramírez-García, J. J., Granados-Correa, F., and Sánchez-Meza, J. C. (2019). Structural and textural influences of surfactant-modified zeolitic materials over the methamidophos adsorption behavior. *Sep. Sci. Technol.* 55 (4), 619–634. doi:10.1080/01496395.2019.1568476

Annett, R., Habibi, H. R., and Hontela, A. (2014). Impact of glyphosate and glyphosate-based herbicides on the freshwater environment. *J. Appl. Toxicol.* 34 (5), 458–479. doi:10.1002/jat.2997

Barolo, G., Livraghi, S., Chiesa, M., Paganini, M. C., and Giamello, E. (2012). Mechanism of the photoactivity under visible light of N-doped titanium dioxide. Charge carriers migration in irradiated N-TiO_2 investigated by electron paramagnetic resonance. *J. Phys. Chem. C* 116 (39), 20887–20894. doi:10.1021/jp306123d

Battaglin, W. A., Meyer, M. T., Kuivila, K. M., and Dietze, J. E. (2014). Glyphosate and its degradation product AMPA occur frequently and widely in U.S. Soils, surface water, groundwater, and precipitation. *JAWRA J. Am. Water Resour. Assoc.* 50 (2), 275–290. doi:10.1111/jawr.12159

Battgalin, W. A., Kolpin, D. W., Scribner, E. A., Kuivila, K. M., and Sandstrom, M. W. (2005). Glyphosate, other herbicides, and transformation products in midwestern Streams,2002. *J. Am. water Resour. Assoc.* 41 (2), 323–332. doi:10.1111/j.1752-1688. 2005.tb03738.x

Bian, Z., Feng, Y., Li, H., Yu, H., and Wu, H. (2021). Adsorption-photocatalytic degradation and kinetic of sodium isobutyl xanthate using the nitrogen and cerium co-doping TiO$_2$-coated activated carbon. *Chemosphere* 263, 128254. doi:10.1016/j. chemosphere.2020.128254

Bonansea, R. I., Filippi, I., Wunderlin, D. A., Marino, D. J. G., and Ame, M. V. (2017). The fate of glyphosate and AMPA in a freshwater endorheic basin: An ecotoxicological risk assessment. *Toxics* 6 (1), 3. doi:10.3390/toxics6010003

Burroughs, P., Hamnett, A., Orchard, A. F., and Thornton, G. (1976). Satellite structure in the X-ray photoelectron spectra of some binary and mixed oxides of lanthanum and cerium. *J. Chem. Soc. Dalton Trans.* 17, 1686. doi:10.1039/dt9760001686

Cao, Y., Fan, Y., Ma, Z., Cheng, Z., Xiang, Q., Duan, Z., et al. (2018). Urea-functionalized SBA-15 hybrids: Post-grafting synthesis, high-performance organophosphorus sensing and their response mechanism. *Sensors Actuators B Chem.* 273, 1162–1169. doi:10.1016/j. snb.2018.04.112

Chaker, H., Fourmentin, S., and Chérif-Aouali, L. (2020). Efficient photocatalytic degradation of ibuprofen under visible light irradiation using silver and cerium Co-doped mesoporous TiO$_2$. *ChemistrySelect* 5 (38), 11787–11796. doi:10.1002/slct. 202002730

Chen, Y., and Liu, K. (2017). Fabrication of Ce/N co-doped TiO$_2$/diatomite granule catalyst and its improved visible-light-driven photoactivity. *J. Hazard Mater* 324, 139–150. doi:10.1016/j.jhazmat.2016.10.043

Choudhury, B., Borah, B., and Choudhury, A. (2013). Ce–Nd codoping effect on the structural and optical properties of TiO$_2$ nanoparticles. *Mater. Sci. Eng. B* 178 (4), 239–247. doi:10.1016/j.mseb.2012.11.017

Coupe, R. H., Kalkhoff, S. J., Capel, P. D., and Gregoire, C. (2012). Fate and transport of glyphosate and aminomethylphosphonic acid in surface waters of agricultural basins. *Pest Manag. Sci.* 68 (1), 16–30. doi:10.1002/ps.2212

Dhanalakshmi, J., Iyyapushpam, S., Nishanthi, S. T., Malligavathy, M., and Pathinettam Padiyan, D. (2017). Investigation of oxygen vacancies in Ce coupled TiO$_2$ nanocomposites by Raman and PL spectra. *Adv. Nat. Sci. Nanosci. Nanotechnol.* 8 (1), 015015. doi:10.1088/ 2043-6254/aa5984

Echavia, G. R., Matzusawa, F., and Negishi, N. (2009). Photocatalytic degradation of organophosphate and phosphonoglycine pesticides using TiO$_2$ immobilized on silica gel. *Chemosphere* 76 (5), 595–600. doi:10.1016/j.chemosphere.2009.04.055

Espinoza-Montero, P. J., Vega-Verduga, C., Alulema-Pullupaxi, P., Fernandez, L., and Paz, J. L. (2020). Technologies employed in the treatment of water contaminated with glyphosate: A review. *Molecules* 25 (23), 5550. doi:10.3390/molecules25235550

Gill, J. P. K., Sethi, N., Mohan, A., Datta, S., and Girdhar, M. (2017). Glyphosate toxicity for animals. *Environ. Chem. Lett.* 16 (2), 401–426. doi:10.1007/s10311-017-0689-0

Hanke, I., Wittmer, I., Bischofberger, S., Stamm, C., and Singer, H. (2010). Relevance of urban glyphosate use for surface water quality. *Chemosphere* 81 (3), 422–429. doi:10.1016/ j.chemosphere.2010.06.067

He, P., Zhao, Z., Tan, Y., E, H., Zuo, M., Wang, J., et al. (2021). Photocatalytic degradation of deoxynivalenol using cerium doped titanium dioxide under ultraviolet light irradiation. *Toxins (Basel)* 13 (7), 481. doi:10.3390/toxins13070481

Hoffman, C. A., and Ronald, C. C. (1995). Can we sustain the biological basis of agriculture? *Annu. Rev. Ecol. Syst.* 26 (1), 69–92. doi:10.1146/annurev.es.26.110195.000441

Hu, H., Lin, Y., and Hu, Y. H. (2019). Synthesis, structures and applications of single component core-shell structured TiO$_2$: A review. *Chem. Eng. J.* 375, 122029. doi:10.1016/j. cej.2019.122029

Ikeda, S., Sugiyama, N., Pal, B., Marcí, G., Palmisano, L., Noguchi, H., et al. (2001). Photocatalytic activity of transition-metal-loaded titanium(IV) oxide powders suspended in aqueous solutions: Correlation with electron–hole recombination kinetics. *Phys. Chem. Chem. Phys.* 3 (2), 267–273. doi:10.1039/b008028o

Jaisi, D. P., Li, H., Wallace, A. F., Paudel, P., Sun, M., Balakrishna, A., et al. (2016). Mechanisms of bond cleavage during manganese oxide and UV degradation of glyphosate: Results from phosphate oxygen isotopes and molecular simulations. *J. Agric. Food Chem.* 64 (45), 8474–8482. doi:10.1021/acs.jafc.6b02608

Jiang, N., Shang, R., Heijman, S. G. J., and Rietveld, L. C. (2018). High-silica zeolites for adsorption of organic micro-pollutants in water treatment: A review. *Water Res.* 144, 145–161. doi:10.1016/j.watres.2018.07.017

Khalid, N. R., Majid, A., Tahir, M. B., Niaz, N. A., and Khalid, S. (2017). Carbonaceous-TiO$_2$ nanomaterials for photocatalytic degradation of pollutants: A review. *Ceram. Int.* 43 (17), 14552–14571. doi:10.1016/j.ceramint.2017.08.143

Lee, H. U., Lee, S. C., Choi, S., Son, B., Lee, S. M., Kim, H. J., et al. (2013). Efficient visible-light induced photocatalysis on nanoporous nitrogen-doped titanium dioxide catalysts. *Chem. Eng. J.* 228, 756–764. doi:10.1016/j.cej.2013.05.059

Liu, C., Tang, X., Mo, C., and Qiang, Z. (2008). Characterization and activity of visible-light-driven TiO$_2$ photocatalyst codoped with nitrogen and cerium. *J. Solid State Chem.* 181 (4), 913–919. doi:10.1016/j.jssc.2008.01.031

López, R., and Gómez, R. (2011). Band-gap energy estimation from diffuse reflectance measurements on sol–gel and commercial TiO$_2$: A comparative study. *J. Sol-Gel Sci. Technol.* 61 (1), 1–7. doi:10.1007/s10971-011-2582-9

Ma, J., Zhu, J., Wang, W., Ruan, P., Rajeshkumar, S., and Li, X. (2019). Biochemical and molecular impacts of glyphosate-based herbicide on the gills of common carp. *Environ. Pollut.* 252, 1288–1300. doi:10.1016/j.envpol.2019.06.040

Maarisetty, D., and Baral, S. S. (2019). Defect-induced enhanced dissociative adsorption, optoelectronic properties and interfacial contact in Ce doped TiO$_2$: Solar photocatalytic degradation of Rhodamine B. *Ceram. Int.* 45 (17), 22253–22263. doi:10.1016/j.ceramint. 2019.07.251

Makdee, A., Unwiset, P., Chayakul Chanapattharapol, K., and Kidkhunthod, P. (2018). Effects of Ce addition on the properties and photocatalytic activity of TiO$_2$, investigated by X-ray absorption spectroscopy. *Mater. Chem. Phys.* 213, 431–443. doi:10.1016/j. matchemphys.2018.04.016

Matějová, L., Kočí, K., Reli, M., Čapek, L., Hospodková, A., Peikertová, P., et al. (2014). Preparation, characterization and photocatalytic properties of cerium doped TiO$_2$: On the effect of Ce loading on the photocatalytic reduction of carbon dioxide. *Appl. Catal. B Environ.* 152-153, 172–183. doi:10.1016/j.apcatb.2014.01.015

Matozzo, V., Munari, M., Masiero, L., Finos, L., and Marin, M. G. (2019). Ecotoxicological hazard of a mixture of glyphosate and aminomethylphosphonic acid to the mussel *Mytilus galloprovincialis* (Lamarck 1819). *Sci. Rep.* 9 (1), 14302. doi:10.1038/ s41598-019-50607-0

Mesnage, R., Defarge, N., Spiroux de Vendomois, J., and Seralini, G. E. (2015). Potential toxic effects of glyphosate and its commercial formulations below regulatory limits. *Food Chem. Toxicol.* 84, 133–153. doi:10.1016/j.fct.2015.08.012

Nasir, M., Bagwasi, S., Jiao, Y., Chen, F., Tian, B., and Zhang, J. (2014). Characterization and activity of the Ce and N co-doped TiO$_2$ prepared through hydrothermal method. *Chem. Eng. J.* 236, 388–397. doi:10.1016/j.cej.2013.09.095

Negishi, N., Sano, T., Hirakawa, T., Koiwa, F., Chawengkijwanich, C., Pimpha, N., et al. (2012). Photocatalytic detoxification of aqueous organophosphorus by TiO$_2$ immobilized silica gel. *Appl. Catal. B Environ.* 128, 105–118. doi:10.1016/j.apcatb.2012.04.039

Oladoja, N. A., Adelagun, R. O. A., Ahmad, A. L., and Ololade, I. A. (2015). Phosphorus recovery from aquaculture wastewater using thermally treated gastropod shell. *Process Saf. Environ. Prot.* 98, 296–308. doi:10.1016/j.psep.2015.09.006

Rajoriya, S., Bargole, S., George, S., Saharan, V. K., Gogate, P. R., and Pandit, A. B. (2019). Synthesis and characterization of samarium and nitrogen doped TiO$_2$ photocatalysts for photo-degradation of 4-acetamidophenol in combination with hydrodynamic and acoustic cavitation. *Sep. Purif. Technol.* 209, 254–269. doi:10.1016/j. seppur.2018.07.036

Ruiz-Toledo, J., Castro, R., Rivero-Perez, N., Bello-Mendoza, R., and Sanchez, D. (2014). Occurrence of glyphosate in water bodies derived from intensive agriculture in a tropical region of southern Mexico. *Bull. Environ. Contam. Toxicol.* 93 (3), 289–293. doi:10.1007/ s00128-014-1328-0

Samsel, A., and Seneff, S. (2013). Glyphosate's suppression of cytochrome P450 enzymes and amino acid biosynthesis by the gut microbiome: Pathways to modern diseases. *Entropy* 15 (12), 1416–1463. doi:10.3390/e15041416

Senthilnathan, J., and Philip, L. (2010). Photocatalytic degradation of lindane under UV and visible light using N-doped TiO$_2$. *Chem. Eng. J.* 161 (1-2), 83–92. doi:10.1016/j.cej. 2010.04.034

Shaari, N., Tan, S. H., and Mohamed, A. R. (2012). Synthesis and characterization of CNT/Ce-TiO$_2$ nanocomposite for phenol degradation. *J. Rare Earths* 30 (7), 651–658. doi:10.1016/s1002-0721(12)60107-0

Sharotri, N., Sharma, D., and Sud, D. (2019). Experimental and theoretical investigations of Mn-N-co-doped TiO$_2$ photocatalyst for visible light induced degradation of organic pollutants. *J. Mater. Res. Technol.* 8 (5), 3995–4009. doi:10.1016/j.jmrt.2019.07.008

Sheals, J., Sjöberg, S., and Persson, P. (2002). Adsorption of glyphosate on goethite: Molecular characterization of surface complexes. *Environ. Sci. Technol.* 36 (14), 3090–3095. doi:10.1021/es010295w

Singaram, B., Varadharajan, K., Jeyaram, J., Rajendran, R., and Jayavel, V. (2017). Preparation of cerium and sulfur codoped TiO$_2$ nanoparticles based photocatalytic activity with enhanced visible light. *J. Photochem. Photobiol. A Chem.* 349, 91–99. doi:10.1016/j. jphotochem.2017.09.003

Spadavecchia, F., Cappelletti, G., Ardizzone, S., Bianchi, C. L., Cappelli, S., Oliva, C., et al. (2010). Solar photoactivity of nano-N-TiO$_2$ from tertiary amine: Role of defects and paramagnetic species. *Appl. Catal. B Environ.* 96 (3-4), 314–322. doi:10.1016/j.apcatb. 2010.02.027

Sun, Z., Pichugin, V. F., Evdokimov, K. E., Konishchev, M. E., Syrtanov, M. S., Kudiiarov, V. N., et al. (2020). Effect of nitrogen-doping and post annealing on wettability and band gap energy of TiO$_2$ thin film. *Appl. Surf. Sci.* 500, 144048. doi:10.1016/j.apsusc.2019. 144048

Suwannaruang, T., Kamonsuangkasem, K., Kidkhunthod, P., Chirawatkul, P., Saiyasombat, C., Chanlek, N., et al. (2018). Influence of nitrogen content levels on structural properties and photocatalytic activities of nanorice-like N-doped TiO$_2$ with various calcination temperatures. *Mater. Res. Bull.* 105, 265–276. doi:10.1016/j. materresbull.2018.05.010

Tang, X., Wang, Z., and Wang, Y. (2018). Visible active N-doped TiO_2/reduced graphene oxide for the degradation of tetracycline hydrochloride. *Chem. Phys. Lett.* 691, 408–414. doi:10.1016/j.cplett.2017.11.037

Tarazona, J. V., Court-Marques, D., Tiramani, M., Reich, H., Pfeil, R., Istace, F., et al. (2017). Glyphosate toxicity and carcinogenicity: A review of the scientific basis of the European union assessment and its differences with IARC. *Arch. Toxicol.* 91 (8), 2723–2743. doi:10.1007/s00204-017-1962-5

Tresnakova, N., Stara, A., and Velisek, J. (2021). Effects of glyphosate and its metabolite AMPA on aquatic organisms. *Appl. Sci.* 11 (19), 9004. doi:10.3390/app11199004

Tu, B., Chen, H., Deng, J., Xue, S., Ma, X., Xu, Y., et al. (2021). Preparation of N-I co-doped TiO_2 supported on activated carbon photocatalyst for efficient photocatalytic reduction of Cr(-) ions. *Colloids Surfaces A Physicochem. Eng. Aspects* 622, 126660. doi:10.1016/j.colsurfa.2021.126660

Van Bruggen, A. H. C., He, M. M., Shin, K., Mai, V., Jeong, K. C., Finckh, M. R., et al. (2018). Environmental and health effects of the herbicide glyphosate. *Sci. Total Environ.* 616-617, 255–268. doi:10.1016/j.scitotenv.2017.10.309

Villamar-Ayala, C. A., Carrera-Cevallos, J. V., Vasquez-Medrano, R., and Espinoza-Montero, P. J. (2019). Fate, eco-toxicological characteristics, and treatment processes applied to water polluted with glyphosate: A critical review. *Crit. Rev. Environ. Sci. Technol.* 49 (16), 1476–1514. doi:10.1080/10643389.2019.1579627

Wang, C., Ao, Y., Wang, P., Hou, J., and Qian, J. (2011a). Preparation of cerium and nitrogen co-doped titania hollow spheres with enhanced visible light photocatalytic performance. *Powder Technol.* 210 (3), 203–207. doi:10.1016/j.powtec.2011.03.015

Wang, N., Hao, L., Chen, J., Zhao, Q., and Xu, H. (2018). Adsorptive removal of organics from aqueous phase by acid-activated coal fly ash: Preparation, adsorption, and fenton regenerative valorization of "spent" adsorbent. *Environ. Sci. Pollut. Res. Int.* 25 (13), 12481–12490. doi:10.1007/s11356-018-1560-y

Wang, Y., Feng, C., Zhang, M., Yang, J., and Zhang, Z. (2011b). Visible light active N-doped TiO_2 prepared from different precursors: Origin of the visible light absorption and photoactivity. *Appl. Catal. B Environ.* 104 (3-4), 268–274. doi:10.1016/j.apcatb.2011.03.020

Xiao, J., Peng, T., Li, R., Peng, Z., and Yan, C. (2006). Preparation, phase transformation and photocatalytic activities of cerium-doped mesoporous titania nanoparticles. *J. Solid State Chem.* 179 (4), 1161–1170. doi:10.1016/j.jssc.2006.01.008

Xu, A., Gao, Y., and Liu, H. (2002). The preparation, characterization, and their photocatalytic activities of rare-earth-doped TiO_2 nanoparticles. *J. Catal.* 207 (2), 151–157. doi:10.1006/jcat.2002.3539

Xu, Y., Chen, H., Zeng, Z., and Lei, B. (2006). Investigation on mechanism of photocatalytic activity enhancement of nanometer cerium-doped titania. *Appl. Surf. Sci.* 252 (24), 8565–8570. doi:10.1016/j.apsusc.2005.11.072

Yu, Y., Wu, R., and Clark, M. (2010). Phosphate removal by hydrothermally modified fumed silica and pulverized oyster shell. *J. Colloid Interface Sci.* 350 (2), 538–543. doi:10.1016/j.jcis.2010.06.033

Zhang, W., Liang, Z., Wang, A., Shu, J., and Hu, m. (2022). Optimized preparation of modified oyster shell powder and its adsorption performance for glyphosate. *Ind. Water Treat.* 42 (03), 90–97.